Usui *et al. Earth, Planets and Space* (2024) 76:47
https://doi.org/10.1186/s40623-024-01980-2

Earth, Planets and Space

FULL PAPER

Open Access

Age constraints on island-arc submarine basalts from geomagnetic paleointensity

Yoichi Usui[1*], Iona McIntosh[2] and Osamu Ishizuka[3]

Abstract

High-resolution dating of volcanic rocks is the foundation for understanding the evolution of volcanoes and for estimating possible hazards. However, dating is often difficult for submarine volcanoes, where radiocarbon or other dating is frequently unavailable or imprecise. Here, we report paleointensity results from submarine basalts around Izu-Oshima Island, a typical island-arc volcano, and their bearing on age constraints. Basaltic lava samples were collected from submarine ridges located southeast of Izu-Oshima Island. Rock magnetic data indicate that the samples contain Ti-rich titanomagnetite with blocking temperatures of around 250–400 °C. The magnetic properties of the samples do not change significantly when heated in Ar or vacuum. We apply the Tsunakawa-Shaw method to estimate absolute paleointensity. Samples from different submarine ridges show distinct behavior. One ridge (SE1) shows moderate paleointensity of about 37 μT, while another ridge (SE3) records relatively strong magnetic fields of about 60 μT. Comparing those results with regional paleointensity data, we estimate the age of the SE1 ridge to be younger than 0.5 ka or around 1.4 ka. The other ridge (SE2) exhibits different paleointensity for two samples obtained from different localities, implying that the ridge consists of multiple eruptions. These results demonstrate that paleomagnetism can improve the dating of submarine volcanic rocks.

Keywords Tsunakawa-Shaw paleointensity, Izu-Oshima Island, Holocene, Secular variation

*Correspondence:
Yoichi Usui
usui-yoichi@se.kanazawa-u.ac.jp
Full list of author information is available at the end of the article

Graphical Abstract

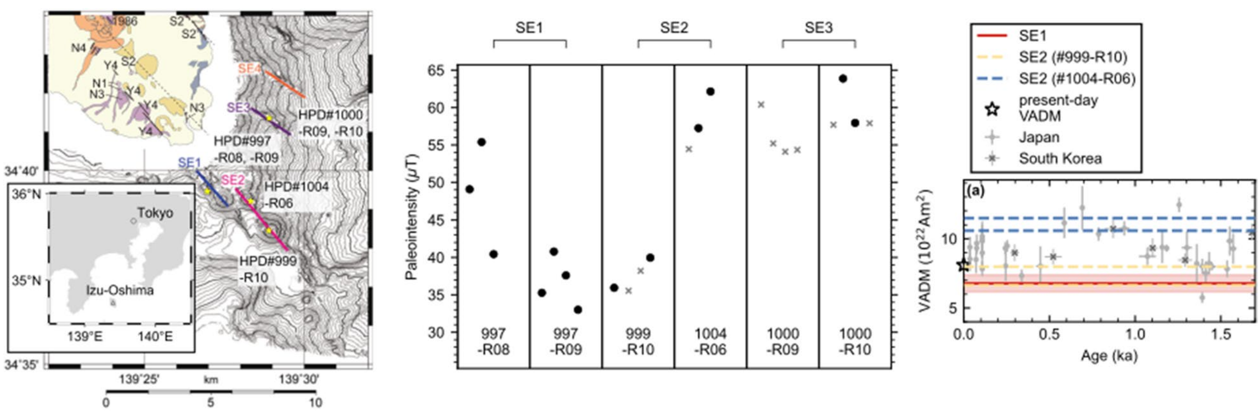

Introduction

Submarine volcanic activity can cause severe disruption to both civilization and natural systems (e.g., Imamura et al. 2022; Ohno et al. 2022). However, submarine eruption history is generally not well known compared to subaerial volcanoes. It is particularly difficult to reconstruct a high-resolution submarine volcanic activity; while detailed radiocarbon dating of associated materials is sometimes applicable to document the activity of subaerial volcanoes over the past few tens of thousands of years (e.g., Kawanabe 2012; Ishizuka et al. 2015), this method is essentially unavailable for submarine volcanic rocks.

Geomagnetic paleosecular variations of both direction and intensity have been utilized to estimate or refine numerical ages for recent volcanic and sedimentary materials (e.g., Greve and Turner 2017; Nitta et al. 2020; Kanamatsu et al. 2022). Submarine samples often lack orientation control, meaning that we cannot determine the paleomagnetic directions. Nevertheless, it has been demonstrated that age estimation for unoriented basaltic glass samples from mid-ocean ridges is possible using paleointensity only (Carlut and Kent 2000; Carlut et al. 2004; Bowles et al. 2006; 2014). Basaltic rocks on the seafloor generally undergo low-temperature oxidation which hampers absolute paleointensity determination due to overprint by thermochemical magnetic remanence (e.g., Grommé et al. 1979; Riisager et al. 2003). On the contrary, the timing of pervasive oxidation is still under debate. From mid-ocean ridge basalt, apparently successful absolute paleointensity results were reported from young pillows with ages spanning a few months (Kent and Gee 1996) to 100 ka (Grommé et al. 1979; Prévot et al. 1983). In addition, marine magnetic anomalies around a spreading ridge revealed patterns consistent with absolute and relative paleointensity data up to 800 ka (Gee et al. 2000), suggesting that most remanence carrier minerals and their thermoremanent magnetization (TRM) may be preserved. Rocks from arc settings have not been examined systematically yet, but we may expect young samples to provide reliable absolute paleointensity.

In this paper, we estimate the paleointensity of submarine lavas around Izu-Oshima Island, a typical island-arc volcano. We compare the results with regional data and global models. Together with age constraints by petrography and geochemistry, we show that paleomagnetism can refine age estimates of these submarine lavas.

Materials

Izu-Oshima volcano

Izu-Oshima volcano is located about 100 km south of Tokyo. The top of the volcano forms an island (Izu-Oshima Island), which is inhabited by ~6000 people. The volcano is at the northernmost part of the Izu-Bonin arc. Written records indicate that the Izu-Oshima volcano has erupted every 100–150 years from the seventh century CE until the mid-nineteenth century, and then every 30–50 years to the present with smaller scale eruptions (Kawanabe 1998). Geological data show that the magmatic activity in the current summit region of Izu-Oshima island goes back to ~20 ka. The activity during the past ~20 kyr has produced satellite cones and eruptive fissures trending NW-SE both on land and in the sea. Petrographic and geochemical analyses of submarine ridges suggest that these edifices were also fed by Izu-Oshima volcano magmas (Ishizuka et al. 2014). Earlier activity began around 50 ka, and its remnant is exposed on the NE flank of the island (Kawanabe 1998).

For submarine activities, limited age constraints have been obtained from petrography and geochemistry. Petrography of both subaerial and submarine volcanic rocks distinguishes plagioclase-phyric and sparsely phyric basalts. Kawanabe (1991) proposed that these two petrography types approximately characterize eruptions before and after a large eruption at 1.8 ka, respectively (Nakamura 1964; Kawanabe 2012), even though the topmost part of the pre-eruption basalt includes aphyric basalt (Kawanabe 1991). Radiocarbon-dated subaerial Izu-Oshima magma spanning the last 14 ka reveals large variation in trace element compositions (in particular Ba, La, Yb, and Ce) and Sr, Nd, and Pb isotope ratios (Ishizuka et al. 2015). Those variations were interpreted to reflect a mixing of frontal arc Izu-Oshima magma with back-arc magma with a smaller slab-derived fluid influx, similar to an adjacent volcanic field. Specifically, the composition was nearly pure frontal-arc component at 14 ka, followed by an increase in the back-arc component until the highest contribution (~ 40%) at around 5.4 ka. Then, the composition rapidly returned to the frontal-arc composition. The submarine rocks reveal a similar compositional range (Ishizuka et al. 2014), suggesting that the geochemical correlation to the subaerial samples can provide crude age estimates.

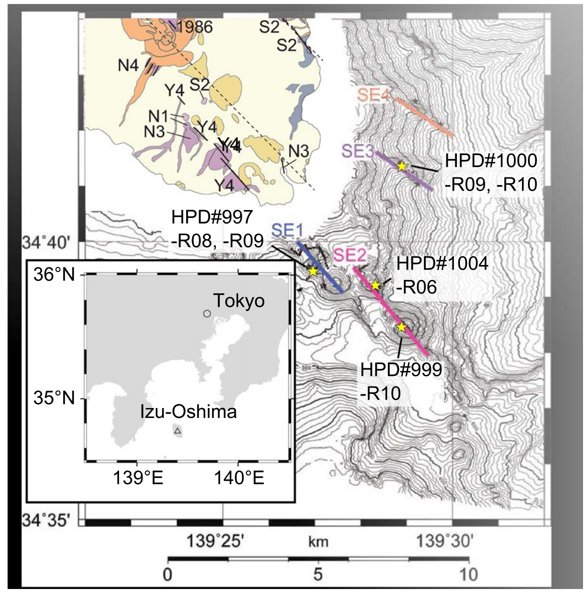

Fig. 1 Sample locations with seafloor bathymetry and simplified subaerial geological map modified from Ishizuka et al. (2014). Bathymetry was obtained by a high-resolution multi-narrow beam echo-sounder survey. Major bathymetry contours are shown in black and 100 m apart, while gray contours are spaced 20 m. Color lines indicate submarine ridges identified by Ishizuka et al. (2014) based on bathymetry. Yellow stars show sample locations. Eruptive fissures on Izu-Oshima Island are shown by black lines with eruption stage names (Kawanabe 1998). Different colors on Izu-Oshima Island indicate the distribution of lavas at different stages. Inset shows the location of Izu-Oshima Island

Samples

We measure samples from submarine ridges (chains of cones) southeast of the Izu-Oshima volcano (Fig. 1). Because the samples are from topographic high, we consider they originated from the corresponding ridge. The samples were obtained using robotic arms of ROV Hyper-Dolphin during NT09-06 (R/V Natsushima) cruise in 2009. We use samples from three ridges namely SE1, SE2, and SE3 (Fig. 1 and Table 1); SE1 and SE3 samples were collected at sites close to each other on each ridge, while SE2 samples were obtained from two sites about 2 km apart. The original rock samples were between 3 and 30 kg each. The activity of the submarine ridges was inferred to be < 14 ka, based on geological observations (Ishizuka et al. 2014). ROV observations and seismic profiles show no sediment cover on the submarine volcanic ridges, suggesting young ages. In particular, the seismic profiles of the submarine ridges indicate that the lavas and volcaniclastics along the ridges are at the same stratigraphic level as the uppermost layer of the southeastern slope of the Izu-Oshima edifice (Irozaki-oki group; Okamura et al. 1999). This stratigraphic correlation indicates that the ridges are as young as subaerial satellite cones (< 14 ka). The samples from SE1 and SE2 are sparsely phyric, suggesting they are younger than ~ 1.8 ka. On the contrary, the samples from SE3 show more abundant plagioclase phenocryst, suggesting it is older than ~ 1.8 ka (Kawanabe 1991; Ishizuka et al. 2014). Their geochemical data were reported by Ishizuka et al. (2014). Samples from each ridge revealed similar compositions, arguing

Table 1 Sample information

Sample name	Latitude (°)	Longitude (°)	Water depth (m)	Ridge	Existing age constraints
HPD#997-R08	34.658	139.450	226	SE1	< 1.8 ka
HPD#997-R09	34.659	139.451	159	SE1	< 1.8 ka
HPD#999-R10	34.641	139.481	226	SE2	< 1.8 ka
HPD#1004-R06	34.653	139.471	214	SE2	< 1.8 ka
HPD#1000-R09	34.688	139.481	404	SE3	> 1.8 ka
HPD#1000-R10	34.689	139.481	369	SE3	> 1.8 ka

against long-term (> 1 kyr) activities. None of our samples show significant back-arc contribution, suggesting that their ages are not around 5.4 ka.

Methods

To infer magnetic mineralogy, we measured the temperature dependence of magnetic susceptibility $k(T)$. Measurements were conducted using the KLY-4 with a furnace CS-3 (AGICO). Powdered samples were heated in flowing Ar up to 700 °C and cooled to 50 °C. Selected samples were also measured in air. Additional measurements were also conducted after the paleointensity experiments. We also measured magnetic hysteresis using a vibrating sample magnetometer (VSM) Model 29/3902 (Princeton measurements) from − 1 to + 1 T. Coercivity of remanence was determined by a backfield demagnetization of isothermal remanence acquired at 1 T.

We used the Tsunakawa-Shaw paleointensity method (Yamamoto et al. 2003) which build upon the Shaw method (Shaw 1974). The method compares the intensity (equivalent moment) of natural remanent magnetization (NRM) and laboratory TRM during alternating field (AF) demagnetizations. Thermal alteration of samples is checked and corrected using the AF demagnetization of anhysteretic remanent magnetization (ARM) before and after heating (Rolph and Shaw 1985). When calculating magnetic moment of each remanence, the remanence vector after the highest AF demagnetization step is subtracted to eliminate the effect of any remaining high coercivity component. The moment of the two ARMs is referred to as M_{ARM0} and M_{ARM1}, respectively. An alteration correction to the moment of the laboratory TRM (M_{TRM1}) is done at each AF demagnetization step as follows:

$$M_{TRM1}{}^{*} = M_{TRM1} \times M_{ARM0} / M_{ARM1} \quad (1)$$

The paleofield intensity (B_{anc}) is estimated as follows:

$$B_{anc} = slope_{NRM-TRM1*} \times B_{lab} \quad (2)$$

where $slope_{NRM\text{-}TRM1*}$ is the gradient from plots of the moment of NRM (M_{NRM}) and $M_{TRM1}{}^{*}$, and B_{lab} is the laboratory field intensity.

The validity of the correction is checked by imparting another set of TRM and ARM (Tsunakawa and Shaw 1994), whose intensities are labeled as M_{TRM2} and M_{ARM2}, respectively. M_{TRM2} is corrected similarly to (1) as

$$M_{TRM2}{}^{*} = M_{TRM2} \times M_{ARM1} / M_{ARM2} \quad (3)$$

A large deviation from unity in the slope of the M_{TRM1}—$M_{TRM2}{}^{*}$ plot would indicate that the correction is invalid for the corresponding specimen.

Samples were cut into 3 or 4 mutually oriented cube specimens of around $1 \times 1 \times 1$ cm^3 size. We could not cut out cubes from the sample HPD#997-R08; instead, we used unoriented small chips mounted on a glass plate with OMEGA CC high-temperature cement.

Paleointensity experiments were conducted in Japan Agency for Marine-Earth Science and Technology. We use spinner magnetometers ASPIN (Natsuhara Giken Co., Ltd.) and JR-6A (AGICO) and cryogenic magnetometers (2G Enterprises). The moment resolutions are around 10^{-8} Am^2, 10^{-10} Am^2, and 10^{-11} Am^2, respectively. AF demagnetization was conducted progressively up to a peak AF of 150 mT using a two-axis sample tumbling demagnetizer DEM-95 (Natsuhara Giken Co., Ltd.). Before a progressive AF demagnetization, we applied a low-temperature demagnetization by putting samples in liquid nitrogen in a magnetic shield to reduce remanence carried by multidomain magnetite (Yamamoto et al. 2003). We imparted TRMs with an applied field of 50 μT using a thermal demagnetization oven TDS-1 (Natsuhara Giken Co., Ltd.). Heating was conducted in a vacuum (< 10 Pa), which would minimize alteration during heating for some samples (Mochizuki et al. 2004). We chose 50 μT to mimic the expected paleointensity for the recent past in Japan (Kitahara et al. 2018, 2021). The maximum temperature was set as 500 °C based on the susceptibility measurements, as detailed later. The holding time was ~ 15 min for the first heating and ~ 1 h for the second. We imparted ARMs using DEM-95 with a DC bias field of 70 μT. The DC field intensity was chosen so that ARM and TRM become comparable magnitudes based on pilot specimens.

We filtered the paleointensity estimates by the following criteria, which are similar to those of Ahn and Yamamoto (2019):

1. A characteristic remanence (ChRM) is isolated from NRM by a progressive AF demagnetization on the orthogonal vector plot.
2. On the M_{NRM} –$M_{TRM1}{}^{*}$ diagram, a linear segment exists within the coercivity range defining the ChRM. The segment should cover at least 30% of the total NRM intensity and should have a correlation coefficient ($R_{NRM-TRM1*}$) larger than 0.995.
3. On the M_{TRM1}–$M_{TRM2}{}^{*}$ diagram, a linear segment with a correlation coefficient ($R_{TRM1-TRM2*}$) larger than 0.995 is recognized in the coercivity range covering that of the linear segment on the M_{NRM} –$M_{TRM1}{}^{*}$ diagram. The high coercivity end of the linear segment on the M_{TRM1}–$M_{TRM2}{}^{*}$ diagram coincides with that of the linear segment on the M_{NRM} –$M_{TRM1}{}^{*}$ diagram. The slope of the linear segment

on the M_{TRM1}–$M_{TRM2}{}^{*}$ diagram ($slope_{TRM1-TRM2*}$) is between 0.95 and 1.05.

The ChRM vector was calculated by principal component analysis (PCA) (Kirschvink 1980).

Results

Rock magnetism

Figure 2 shows $k(T)$ curves. All examined samples heated in Ar show a susceptibility drop at around 300 °C with nearly reversible behavior. Samples HPD#997-R08 and HPD#1004-R06 show a broader reduction in magnetic susceptibility extending to ~ 450 °C. From visual inspections, we interpret that the Curie temperatures of the samples are roughly 300–450 °C. In contrast, samples heated in air reveal highly irreversible curves (Fig. 2g). Based on these results, we performed Tsunakawa–Shaw experiments with a maximum temperature of 500 °C in a vacuum to impart full TRM. The heating curves for samples after the paleointensity experiments show a small contribution of phase(s) with a Curie temperature up to ~ 510 °C (Fig. 2h). This contribution disappears when heated in Ar to 700 °C.

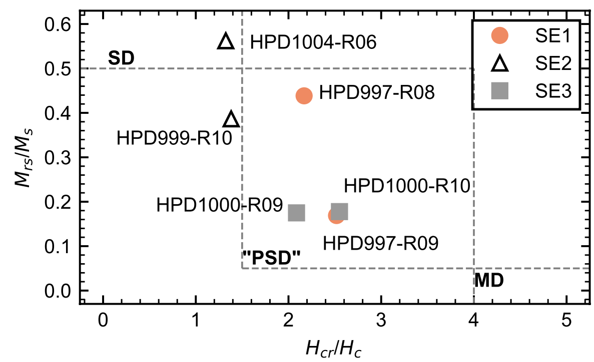

Fig. 3 Day plot showing hysteresis properties. Dashed lines indicate empirically determined diagnostic values of magnetic domain state for titanomagnetite (Day et al. 1997; Dunlop 2002). MD stands for multidomain, PSD for pseudo single domain, and SD for single domain

Hysteresis parameters are summarized on a Day plot (Day et al. 1977; Dunlop 2002) in Fig. 3. Most samples are within the “pseudo-single domain” region to the single-domain region, suggesting a relatively small grain size of magnetic minerals.

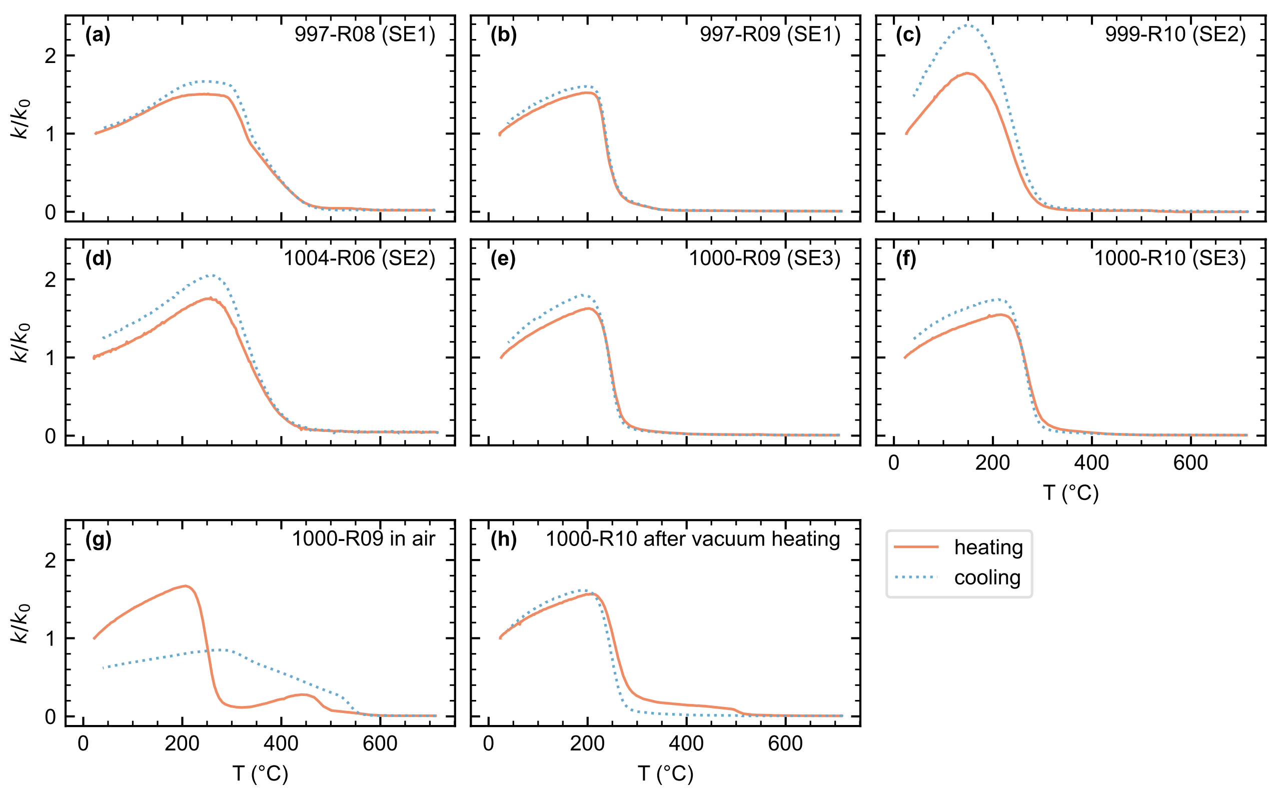

Fig. 2 Temperature dependence of magnetic susceptibility (k). Data are normalized by the room temperature susceptibility before heating (k_0). Orange solid lines show heating curve, and blue dashed lines show cooling curve. **a**–**f** Heating in Ar. **g** Heating in air for the sample HPD#1000-R09. **h** Heating in Ar after paleointensity experiment involving heating to 500 °C in vacuum for the sample HPD#1000-R10

Paleointensity

Each specimen reveals near single-component of NRM during AF demagnetization; however, close examination often reveals a small but persistent overprint demagnetized by fields up to 15–40 mT (Fig. 4a, b). Stability against AF demagnetization is variable, with the median destructive field ranging from 14 to 67 mT (Table 2). Except for the mutually unoriented specimen of HPD#997-R08, the specimens exhibit internally consistent directions for each samples (Fig. 4c).

Representative paleointensity results are shown in Figs. 5, 6. The $M_{NRM} - M_{TRM1}$ plot is mostly straight. ARMs after each heating also reveal minimal alterations, as indicated by high linearity and slopes around 1 in the

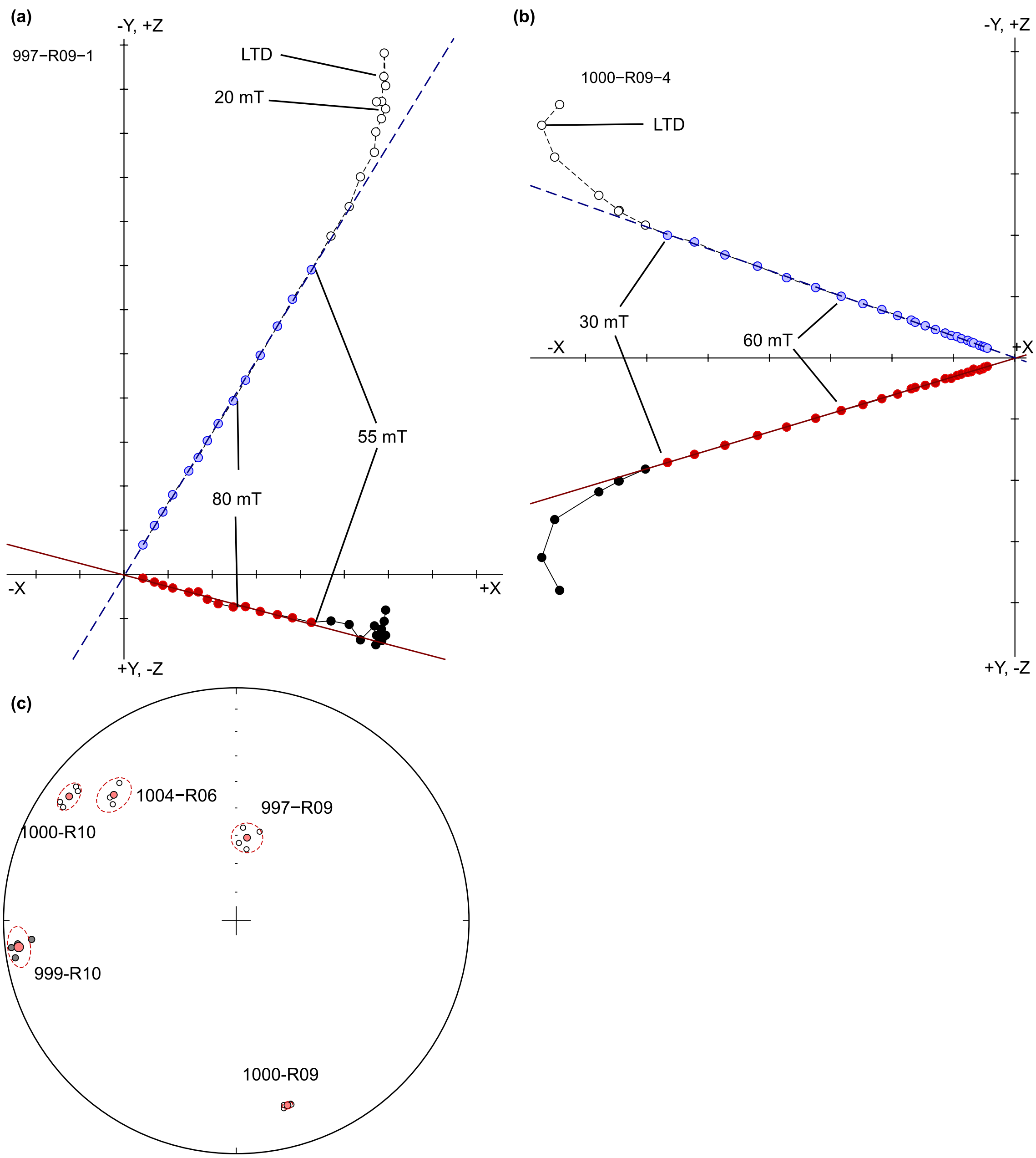

Fig. 4 NRM demagnetizations. Orthogonal vector plots for samples **a** HPD#997-R09 and **b** HPD#1000-R09. Black and red circles represent projections onto the horizontal plane, and white and blue circles to the vertical plane. Colored symbols show steps used to identify ChRM. Dotted lines are the ChRM directions. **c** ChRM direction plotted by equal area projection. Open circles show specimen data. Orange circles show mean directions, with α_{95} indicated by dashed ovals. Note that the samples were not geographically oriented, and the direction of each sample is arbitrary. Plotted with MagePlot (Hatakeyama 2018)

Table 2 NRM demagnetization data

Sample	Specimen	L (mT)	H (mT)	MAD of ChRM (°)	MDF (mT)	Comment
HPD#997-R08	1	0.1	150	4.005	32.9	Unoriented, small chip
HPD#997-R08	2	0	150	3.479	40.5	Unoriented, small chip
HPD#997-R08	3	0	150	6.103	39.6	Unoriented, small chip
HPD#997-R09	1	55	150	1.209	67.4	
HPD#997-R09	2	40	150	0.515	59.6	
HPD#997-R09	3	40	150	0.448	53.8	
HPD#997-R09	4	55	150	1.242	50.6	
HPD#999-R10	1	25	150	1.636	20.2	
HPD#999-R10	2	20	150	1.676	19.7	
HPD#999-R10	3	30	150	2.754	21.7	
HPD#999-R10	4	30	150	2.486	20.5	
HPD#1004-R06	1	30	150	0.411	64.7	
HPD#1004-R06	2	35	150	0.289	49.9	
HPD#1004-R06	3	15	150	0.262	58.5	
HPD#1000-R09	1	15	150	0.879	28.8	
HPD#1000-R09	2	25	150	0.393	50.3	
HPD#1000-R09	3	20	150	0.601	41	
HPD#1000-R09	4	30	150	0.413	44.8	
HPD#1000-R10	1	15	150	0.712	39.3	
HPD#1000-R10	2	15	150	3.837	24.5	
HPD#1000-R10	3	15	150	2.276	13.6	
HPD#1000-R10	4	30	150	2.948	20.6	

L lower field end for the PCA calculation. *H* higher field end for the PCA calculation, *MAD* maximum angular deviation, *MDF* median destructive field

M_{ARM1}—M_{ARM0} and M_{ARM2}—M_{ARM1} plots (Table 3). Thirteen out of 22 specimens pass the selection criteria. Of nine failed specimens, eight specimens showed $slope_{TRM1-TRM2}{}^{*}$ larger than 1, and one revealed $R_{TRM1-TRM2^{*}}$ below 0.995 (Table 3; Fig. 6).

Ridges exhibit different paleointensity characters. Specimens from two sites on the ridge SE1 show a paleofield intensity of 33–55 μT, while specimens from two sites on the ridge SE3 consistently show a higher value of 58–64 μT (Table 3; Fig. 7). At the sample level, HPD#997-R08 show a large scatter (Table 3; Fig. 7), even though we do not detect a major difference in rock magnetic properties relative to the other samples. Based on these observations, we discard the results from HPD#997-08 and use HPD#997-R09 data as representative paleointensity for SE1, which yield the average paleointensity of 36.7 μT. For SE2, the sample HPD#999-R10 yields a paleointensity of 35–40 μT, while HPD#1004-R06 reveals 54–62 μT.

Discussion

Magnetic mineralogy

A prerequisite for absolute paleointensity experiments is that NRM is TRM. The linear relationship in the M_{NRM}–M_{TRM1} plots (Fig. 5) suggests that NRM has similar coercivity distribution with TRM. Additional lines of evidence were obtained from rock magnetic results. Basaltic rocks may undergo low- and high-temperature oxidation, causing secondary thermochemical remanence. Low-temperature oxidation would produce titanomaghemite below its Curie temperature. In our samples, the reversible $k(T)$ curves and minimal changes in ARMs during paleointensity experiments argue against a significant contribution from titanomaghemite, as this mineral would invert into hematite or magnetite upon heating. This observation suggests that the samples examined here preserve TRM acquired during initial cooling. Previous paleomagnetic studies of subaerial lavas from Izu-Oshima Island reported two Curie temperatures of 500–600 °C and 250–350 °C (Tanaka 1982; Yoshihara et al. 2003; Mochizuki et al. 2004). Based on microscopic observations, Mochizuki et al. (2004) suggested that these Curie temperatures correspond to Ti-poor and Ti-rich titanomagnetite, respectively, and that the Ti-poor titanomagnetite originates from high-temperature oxidation of the Ti-rich titanomagnetite. Such Ti-poor titanomagnetite sometimes acquires thermochemical remanence, which may bias paleointensity estimates (Yamamoto et al. 2003; Mochizuki et al. 2004; Fabian 2009). In contrast, our submarine basalts only show the lower Curie temperature, suggesting the lack of high-temperature oxidation of

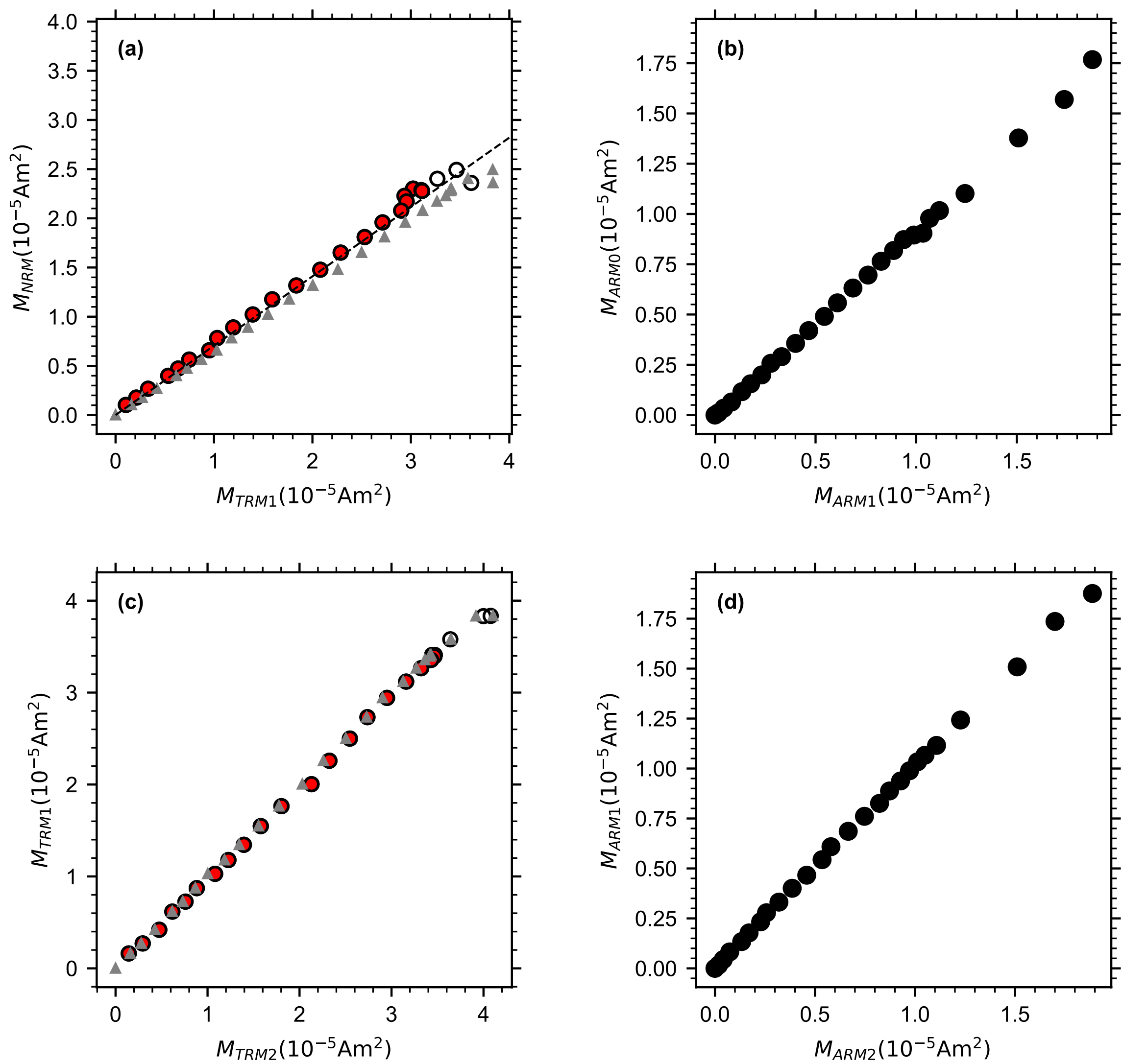

Fig. 5 Example of paleointensity results that met the criteria (HPD#997-R09-01). **a** M_{NRM}–M_{TRM1} diagram. **b** M_{ARM0}–M_{ARM1} diagram. **c** M_{TRM1}–M_{TRM2} diagram. **d** M_{ARM1}–M_{ARM2} diagram. Gray triangles in **a** and **c** show M_{TRM1} and M_{TRM2} before the correction, while circles indicate the corrected TRM intensities (see text for details). Red circles show data used to calculate paleointensity

titanomagnetite. On the basis of the absence of significant low- and high-temperature oxidation, we consider that the NRMs measured here mainly reflect TRMs, even though we cannot completely rule out some contribution from thermochemical remanence.

Heating in a vacuum at 500 °C for ~ 1 h produces some phase(s) with Curie temperature of ~ 510 °C (Fig. 2h). This behavior may reflect slight oxidation of titanomagnetite to titanomaghemite during the experiment. Titanomaghemite may be reduced back to titanomagnetite by small impurity in Ar gas during the subsequent susceptibility measurements. On the contrary, simple oxidation does not explain the result that the new Curie temperature is different from that of the samples heated in air (490–500 °C; Fig. 2g). A possible mechanism to explain these observations is nanoscale chemical clustering (Jackson and Bowles 2018; Bowles et al. 2019). It is reported that some titanomagnetites exhibit Curie temperature enhancement after annealing. However, the reported annealing temperatures tend to be lower than those of our experiments. It is also difficult to account for the fact that the bulk of the samples keep the original Curie temperature. Regardless of the origin, the success in the Tsunakawa-Shaw experiments, in particular the high linearity of M_{NRM} –$M_{TRM1}{}^{*}$ plots, suggests that the high Curie temperature phase(s) does not contribute significantly to the remanence.

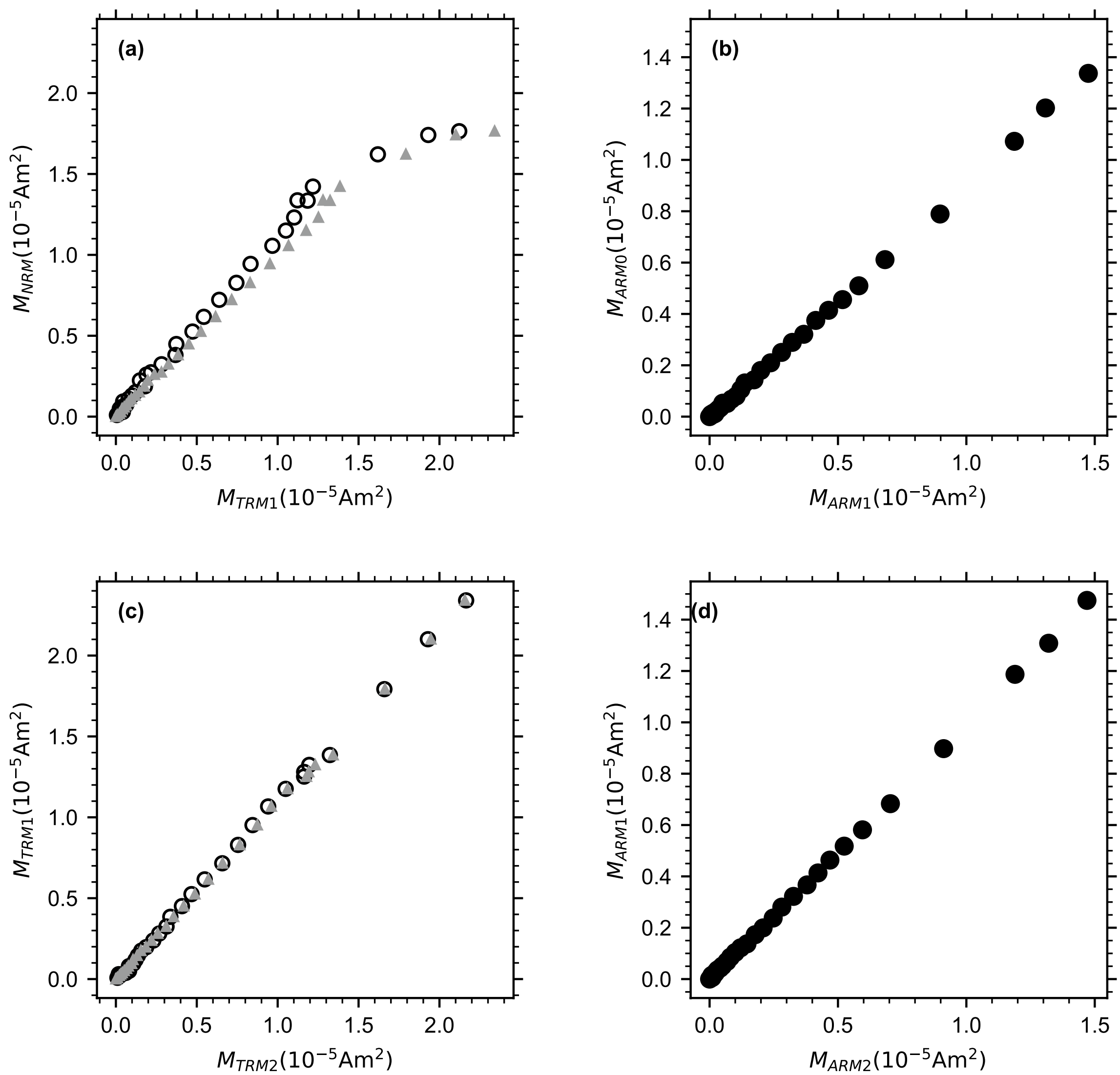

Fig. 6 Example of rejected paleointensity results (HPD#1000-R09-04). **a** M_{NRM}–M_{TRM1} diagram. **b** M_{ARM0}–M_{ARM1} diagram. **c** M_{TRM1}–M_{TRM2} diagram. **d** M_{ARM1}–M_{ARM2}diagram. Gray triangles in **a** and **c** show M_{TRM1} and M_{TRM2} before the correction, while circles indicate the corrected TRM intensities (see text for details). This specimen failed because the slope in **c** is larger than 1.05

Age constraints

To obtain age constraints from our paleointensity data, we compare them with regional compilations from the GEOMAGIA50.v3 database (Brown et al. 2015) as well as global field models (Fig. 8). From the GEOMAGIA50.v3, we select data from Japan and South Korea. The data selections are based on the following four criteria: (1) the paleointensity experiments should have accompanying alteration checks, (2) the number of accepted paleointensity results should be 3 or larger, (3) the standard deviation of the paleointensity should be smaller than 10 μT, and (4) the uncertainty of the age should be smaller than 50 yr (Fig. 8a). We also filter out the data with no error estimates for either age or paleointensity. These criteria return 29 records (Yoshihara et al. 2003; Mochizuki et al. 2004; Yamamoto and Hoshi 2008; Yu 2012; Hong et al. 2013; Kitahara et al. 2018, 2021). Besides, we also incorporated recent archeointensity data from Tema et al. (2023) which meet the above criteria. Data were converted into virtual axial dipole moment (VADM) using the site locations (Table 4).

The SE1 samples indicate relatively low paleointensity values of ~ 37 μT (Table 3, Fig. 7). At the same time, their sparsely phyric petrography suggests that they are likely to be younger than 1.8 ka (Kawanabe 1991, 2012). This petrologic constraint is also consistent with the

Table 3 Tsunakawa–Shaw paleointensity data

Sample	First heating									Second heating							Sample average paleointensity (μT)	Standard deviation (μT)
	Specimen	Ridge	L (mT)	*H* (mT)	$R_{NRM\text{-}TRM1^*}$	$Slope_{NRM\text{-}TRM1^*}$	$R_{ARM0\text{-}ARM1}$	$slope_{ARM0\text{-}ARM1}$	NRM fraction	B_{anc} (μT)	*L* (mT)	H (mT)	$R_{NRM1\text{-}TRM2^*}$	$Slope_{TRM1\text{-}TRM2^*}$	$R_{ARM1\text{-}ARM2}$	$Slope_{ARM1\text{-}ARM2}$		
HPD#997-R08	1	SE1	0.1	150	0.998	0.981	0.997	1.084	1.10	49.1	0	150	0.998	1.017	0.998	0.995		
HPD#997-R08	2	SE1	0	150	0.997	1.108	0.997	1.026	0.97	55.4	0	150	0.999	1.043	0.999	0.969		
HPD#997-R08	3	SE1	0	150	1.000	0.809	0.999	0.982	1.10	40.4	0	150	0.999	1.034	0.997	1.097	HPD#997-R08	
HPD#997-R09	1	SE1	55	150	0.999	0.705	0.999	0.918	0.64	35.3	0	150	0.999	0.976	1.000	1.009	48.3	7.5
HPD#997-R09	2	SE1	40	150	0.999	0.816	1.000	0.935	0.85	40.8	5	150	1.000	1.036	1.000	0.999		
HPD#997-R09	3	SE1	40	150	0.999	0.752	1.000	0.936	0.76	37.6	0.1	150	1.000	0.998	1.000	1.000	HPD#997-R09	
HPD#997-R09	4	SE1	55	150	0.997	0.660	1.000	0.938	0.45	33.0	0	150	1.000	0.995	1.000	1.001	36.7	3.3
HPD#999-R10	1	SE2	25	150	0.999	0.719	1.000	0.965	0.44	35.9	0	150	1.000	1.009	0.998	0.994		
HPD#999-R10	2	SE2	20	150	0.997	0.711	0.998	0.940	0.56	35.5	0	150	0.999	1.050	0.996	1.011		
HPD#999-R10	3	SE2	30	150	0.999	0.764	1.000	0.908	0.34	38.2	0	150	1.000	1.072	0.998	1.003	HPD#999-R10	
HPD#999-R10	4	SE2	30	150	0.996	0.799	0.998	0.925	0.37	40.0	0	150	1.000	1.031	0.998	0.987	38.0	NA
HPD#1004-R06	1	SE2	30	150	1.000	1.089	0.999	0.966	1.00	54.4	0	150	0.998	1.063	1.000	0.964		
HPD#1004-R06	2	SE2	35	150	0.999	1.145	0.999	1.021	0.86	57.3	0.1	150	1.000	1.049	0.999	0.975	HPD#1004-R06	
HPD#1004-R06	3	SE2	15	150	1.000	1.243	0.999	0.921	1.03	62.2	0.1	150	1.000	1.035	1.000	0.993	59.7	NA
HPD#1000-R09	1	SE3	15	150	0.994	1.208	0.999	0.927	0.32	60.4	5	150	0.997	1.050	1.000	0.995		
HPD#1000-R09	2	SE3	25	150	0.999	1.104	1.000	0.906	0.55	55.2	0	150	0.999	1.090	1.000	0.979		
HPD#1000-R09	3	SE3	20	150	0.997	1.082	0.999	0.922	0.38	54.1	10	150	0.995	1.070	0.995	0.989	HPD#1000-R09	
HPD#1000-R09	4	SE3	30	150	0.998	1.087	0.999	0.898	0.54	54.4	0	150	0.999	1.093	1.000	0.973	NA	NA
HPD#1000-R10	1	SE3	15	150	0.998	1.154	1.000	0.913	0.64	57.7	0.1	150	0.999	1.065	1.000	0.952		
HPD#1000-R10	2	SE3	20	150	0.998	1.278	0.999	0.930	0.38	63.9	0	150	0.996	1.027	0.999	0.936		
HPD#1000-R10	3	SE3	20	150	0.997	1.159	0.998	0.966	0.42	58.0	0.1	150	0.995	0.985	0.999	0.939	HPD#1000-R10	
HPD#1000-R10	4	SE3	30	150	0.996	1.158	0.997	0.904	0.33	57.9	0	150	0.990	1.028	0.999	0.940	60.9	NA

L lower field end for the calculation, *H* Higher field end for the calculation, *R* correlation coefficient, B_{anc} Estimated paleointensity (μT). Black bold italic signifies values that failed the criteria and the corresponding paleointensity

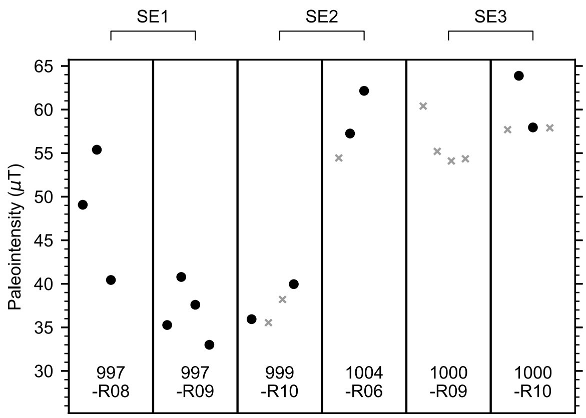

Fig. 7 Summary of the paleointensity results. Solid small circles show data that passed the selection criteria, and gray crosses show data that failed

nearly pure frontal-arc composition, which may occur either < 2 ka or > 10 ka (Ishizuka et al. 2015). Previous paleointensity data from Japan and Korea indicate higher paleointensity between 2 and 1.5 ka and between 0.9 and 0.6 ka, respectively (Hong et al. 2013; Yoshihara et al. 2003; Kitahara et al. 2018, 2021) (Fig. 8a). Thus, our paleointensity data narrow down the possible ages of SE1 to be either younger than 0.5 ka, or around 1.4 ka.

The two samples from the SE2 ridge do not show coherent paleointensities. While these samples show slight difference in Curie temperature and hysteresis parameters (Figs. 2, 3), there is no clear correlation between these rock magnetic properties and paleointensity in the studied samples. Although the number of specimens that pass the selection criteria is not high for SE2, the nominal paleointensities from specimens that failed the criteria show a similar trend (Fig. 7). In contrast to SE1 and SE3, the two samples are obtained from separate sites. We attribute the difference to a change in geomagnetic field between the eruptions, implying that the SE2 ridge consists of products of more than one eruption event. The sparsely phyric petrography and frontal-arc chemical composition point to relatively young (< 1.8 ka) ages for both samples. The sampling site of HPD#1004-R06 locates on the extension of the subaerial Y4 fissure (Fig. 1), whose activity was correlated to a written record at 1421 CE (Kawanabe 1998). Because paleointensity of Y4 lavas (60.6 ± 6.0 μT; Yoshihara et al. 2003) is comparable to that of HPD#1004-R06 (57.3 and 62.2 μT from two specimens), we speculate that HPD#1004-R06 may be simultaneous to the Y4 eruption at 1421 CE. The paleointensity estimated from HPD#999-R10 is close to the SE1 average, which may be correlated to either < 0.5 ka or around 1.4 ka (Fig. 8a).

The global field models reveal possible complications in the age constraints. Here, we consider SHA.DIF.14 k (Pavón-Carrasco et al. 2014) and CALS3k.4 (Korte and ConsTable 2011). The important difference between these two models is that the former is based on volcanic and archeological data, while the latter utilizes

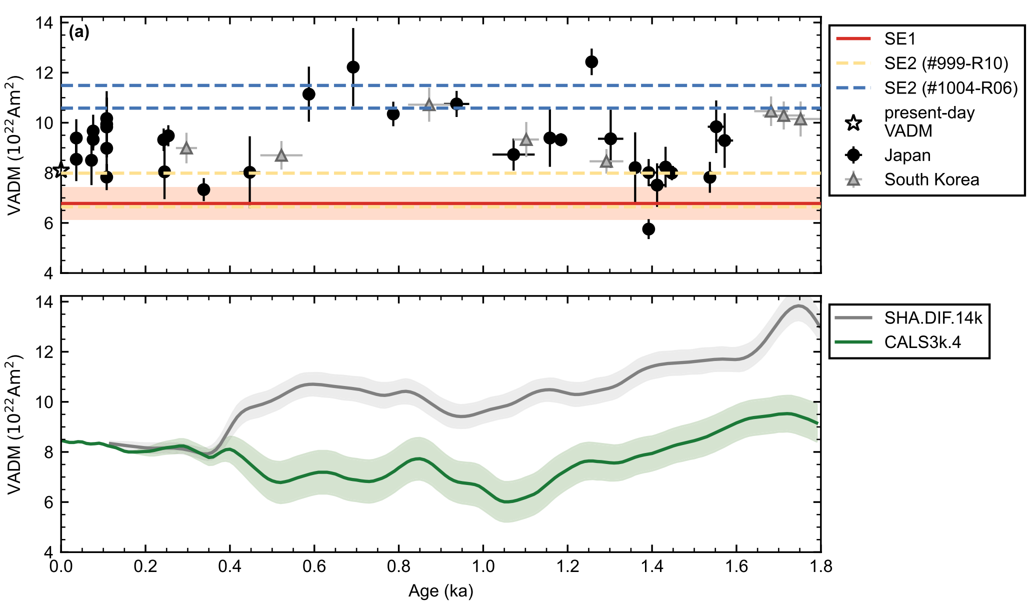

Fig. 8 Comparison with previously published paleointensity results and global models expressed as VADM (virtual axial dipole moment). **a** Comparison with paleointensity data. Data are taken from GEOMAGIA database (Brown et al. 2015) and Tema et al. (2023). See text for the data selection criteria. Red line is the mean VADM from SE1 specimens, with pale red band showing 1σ. Yellow and blue dashed lines show specimen-level paleointensity from two samples from SE2. **b** Comparison with SHA.DIF.14 k model (gray) and CALS3k.4 model (green)

Table 4 VADM

Sample	Specimen	Ridge	Paleointensity (μT)	VADM (10^{22} Am^2)		
HPD#997-R09	1	SE1	35.3	6.5	SE1 average	SE1 σ
HPD#997-R09	2	SE1	40.8	7.5	6.8	0.6
HPD#997-R09	3	SE1	37.6	6.9		
HPD#997-R09	4	SE1	33.0	6.1		
HPD#999-R10	1	SE2	35.9	6.6		
HPD#999-R10	4	SE2	40.0	7.4		
HPD#1004-R06	2	SE2	57.3	10.6		
HPD#1004-R06	3	SE2	62.2	11.5		
HPD#1000-R10	2	SE3	63.9	11.8		
HPD#1000-R10	3	SE3	58.0	10.7		

σ Standard deviation

sedimentary data as well. For the Izu-Oshima location, these two models predict distinct field behavior between 1.8 and 0.4 ka (Fig. 8b). Generally, SHA.DIF.14 k model agrees better with the paleointensity data; however, it overestimates the paleointensity between ~1.0 and 1.5 ka. The data for this period represent the most recent archeointensity studies (Kitahara et al. 2018, 2021, Tema et al. 2023). Tema et al. (2023) proposed that the younger paleointensity data may be biased toward high values, because they are obtained mainly by the Coe–Thellier method (Coe 1967), which may be insufficient to exclude the multidomain contributions. Consequently, they argue that CALS3k.4 model may be more reliable. If this is the case, paleointensity around Japan does not change much during the last 1.8 ka, and the resolving power of paleointensity as a dating tool would be limited. At the same time, some of the South Korean data (Hong et al. 2013) obtained by the IZZI–Thellier method (Yu et al. 2004) as well as our two paleointensities obtained from the sample HPD#1004-R06 are higher than the prediction of CALS3k.4. Reexamination of submarine and subaerial Japanese volcanic rocks is necessary to resolve this issue.

Conclusions

Submarine basaltic lavas from an island-arc volcano provide geomagnetic paleointensity records. Magnetic minerals are Ti-rich titanomagnetites with Curie temperatures of 300–450 °C without detectable low- or high-temperature oxidation. The Tsunakawa-Shaw paleointensity method with vacuum heating is effective in minimizing laboratory alteration during paleointensity experiments in our samples. Two ridges show distinct paleointensity estimates, while another ridge shows lower and higher values. Compared with regional paleosecular variation data, our paleointensity data are consistent with petrographical and geochemical age constraints and narrow the possible age range. For better age constraints, refinement of reference paleointensity data, particularly before 2 ka, is necessary. Our results demonstrate that basaltic rocks from submarine arc volcanoes can retain primary TRM without significant thermochemical overprint for at least a few thousand years. Systematic paleomagnetic studies should be part of future investigations of submarine volcanoes.

Abbreviations

AF	Alternating field
VSM	Vibrating sample magnetometer
NRM	Natural remanent magnetization
ARM	Anhysteretic remanent magnetization
TRM	Thermoremanent magnetization
VADM	Virtual axial dipole moment

Acknowledgements
We thank an anonymous reviewer for providing SHA.DIF.14k data. YU thanks Agri Irisawa for help in the demagnetization experiments.

Author contributions
YU contributed to the conceptualization, formal analysis, investigation, and writing original draft. Iona McIntosh contributed to the conceptualization and review and editing the draft. OI contributed to providing samples and review and editing the draft.

Funding
This study is partly supported by JSPS KAKENHI Grant Numbers JP19H01997 and JP20K14586.

Availability of data and materials
All data will be uploaded to Zenodo repository at. https://doi.org/10.5281/zenodo.10605943.

Declarations

Ethics approval and consent to participate
Not applicable.

Consent for publication
Not applicable.

Competing interests
The authors declare that they have no competing interests.

Author details
[1]College of Geosciences and Civil Engineering, Kanazawa University, Nu-7, Kakuma, Kanazawa, Ishikawa 920-1192, Japan. [2]Volcanoes and Earth's Interior Research Center, Research Institute for Marine Geodynamics, Japan Agency

for Marine-Earth Science and Technology, 2-15 Natsushima-cho, Yokosuka, Kanagawa 237-0061, Japan. [3]Research Institute of Earthquake and Volcano Geology, Geological Survey of Japan, AIST, Central 7, 1-1-1, Higashi, Tsukuba, Ibaraki 305-8567, Japan.

Received: 10 January 2023 Accepted: 9 February 2024
Published online: 22 March 2024

References

Ahn HS, Yamamoto Y (2019) Paleomagnetic study of basaltic rocks from Baengnyeong Island, Korea: efficiency of the Tsunakawa-Shaw paleointensity determination on non-SD-bearing materials and implication for the early Pliocene geomagnetic field intensity. Earth Planets Space 71:126. https://doi.org/10.1186/s40623-019-1107-6

Bowles J, Gee JS, Kent DV, Perfit MR, Soule SA, Fornari DJ (2006) Paleointensity applications to timing and extent of eruptive activity, 9–10 N East Pacific Rise. Geochem Geophys Geosyst 7:Q0600. https://doi.org/10.1029/2005GC001141

Bowles JA, Colman A, McClinton JT, Sinton JM, White SM, Rubin KH (2014) Eruptive timing and 200 year episodicity at 92° W on the hot spot-influenced galapagos spreading center derived from geomagnetic paleointensity. Geochem Geophys Geosyst 15(6):2211–2224. https://doi.org/10.1002/2014GC005315

Bowles JA, Lappe SC, Jackson MJ, Arenholz E, van der Laan G (2019) Curie temperature enhancement and cation ordering in titanomagnetites: evidence from magnetic properties, XMCD, and Mössbauer spectroscopy. Geochem Geophys Geosyst 20(5):2272–2289. https://doi.org/10.1029/2019GC008217

Brown MC, Donadini F, Korte M, Nilsson A, Korhonen K, Lodge A, Lengyel AN, Constable CG (2015) GEOMAGIA50 v3: 1 general structure and modifications to the archeological and volcanic database. Earth Planets Space 67:83. https://doi.org/10.1186/s40623-015-0232-0

Carlut J, Kent DV (2000) Paleointensity record in zero-age submarine basalt glasses: testing a new dating technique for recent MORBs. Earth Planet Sci Lett 183(3–4):389–401. https://doi.org/10.1016/S0012-821X(00)00291-0

Carlut J, Cormier MH, Kent DV, Donnelly KE, Langmuir CH (2004) Timing of volcanism along the northern East Pacific Rise based on paleointensity experiments on basaltic glasses. J Geophys Res Solid Earth. https://doi.org/10.1029/2003JB002672

Coe RS (1967) Paleo-intensities of the earth's magnetic field determined from Tertiary and Quaternary rocks. J Geophys Res 72(12):3247–3262. https://doi.org/10.1029/JZ072i012p03247

Day R, Fuller M, Schmidt VA (1977) Hysteresis properties of titanomagnetites: grain-size and compositional dependence. Phys Earth Planet Inter 13:260–267. https://doi.org/10.1016/0031-9201(77)90108-X

Dunlop DJ (2002) Theory and application of the Day plot (Mrs/Ms versus Hcr/Hc) 1 theoretical curves and tests using titanomagnetite data. J Geophys Res. https://doi.org/10.1029/2001JB000486

Fabian K (2009) Thermochemical remanence acquisition in single-domain particle ensembles: a case for possible overestimation of the geomagnetic paleointensity. Geochem Geophys Geosyst. https://doi.org/10.1029/2009GC002420

Gee JS, Cande SC, Hildebrand JA, Donnelly K, Parker RL (2000) Geomagnetic intensity variations over the past 780 kyr obtained from near-seafloor magnetic anomalies. Nature 408(6814):827–832

Greve A, Turner GM (2017) New and revised palaeomagnetic secular variation records from post-glacial volcanic materials in New Zealand. Phys Earth Planet Inter 269:1–17. https://doi.org/10.1016/j.pepi.2017.05.009

Grommé S, Mankinen EA, Marshall M, Coe RS (1979) Geomagnetic paleointensities by the Thelliers method from submarine pillow basalts: effects of seafloor weathering. J Geophys Res Solid Earth 84(B7):3553–3575

Hatakeyama T (2018) Online plotting applications for paleomagnetic and rock magnetic data. Earth Planets Space 70:139. https://doi.org/10.1186/s40623-018-0906-5

Hong H, Yu Y, Lee CH, Kim RH, Park J, Doh SJ, Kim W, Sung H (2013) Globally strong geomagnetic field intensity circa 3000 years ago. Earth Planet Sci Lett 383:142–152. https://doi.org/10.1016/j.epsl.2013.09.043

Imamura F, Suppasri A, Arikawa T, Koshimura S, Satake K, Tanioka Y (2022) Preliminary observations and impact in Japan of the tsunami caused by the Tonga volcanic eruption on January 15, 2022. Pure Appl Geophys 179:1549–1560. https://doi.org/10.1007/s00024-022-03058-0

Ishizuka O, Geshi N, Kawanabe Y, Ogitsu I, Taylor RN, Tuzino T, Sakamoto I, Arai K, Nakano S (2014) Long-distance magma transport from arc volcanoes inferred from the submarine eruptive fissures offshore Izu-Oshima volcano, Izu-Bonin arc. J Volcanol Geoth Res 285:1–17. https://doi.org/10.1016/j.jvolgeores.2014.08.006

Ishizuka O, Taylor RN, Geshi N, Oikawa T, Kawanabe Y, Ogitsu I (2015) Progressive mixed-magma recharging of Izu-Oshima volcano, Japan: a guide to magma chamber volume. Earth Planet Sci Lett 430:19–29. https://doi.org/10.1016/j.epsl.2015.08.004

Jackson M, Bowles J (2018) Malleable curie temperatures of natural titanomagnetites: Occurrences, modes, and mechanisms. J Geophys Res Solid Earth 123(2):921–940. https://doi.org/10.1002/2017JB015193

Kanamatsu T, Ikehara K, Hsiung KH (2022) Stratigraphy of deep-sea marine sediment using paleomagnetic secular variation: refined dating of turbidite relating to giant earthquake in Japan Trench. Mar Geol 443:106669. https://doi.org/10.1016/j.margeo.2021.106669

Kawanabe Y (1991) Petrological evolution of Izu Oshima volcano. Bull Volc Soc Japan 36(2):297–310. https://doi.org/10.18940/kazan.36.2_297

Kawanabe Y (2012) New 14C ages of the Younger Oshima Group, Izu-Oshima volcano, Izu-Ogasawara arc, Japan. Bull Geo Survey Japan 63:283–289. https://doi.org/10.9795/bullgsj.63.283

Kawanabe Y (1998) Geological map of Izu-Oshima volcano. Geological Map of Volcano 10. Geological Survey of Japan, Tsukuba, Japan.

Kent DV, Gee J (1996) Magnetic alteration of zero-age oceanic basalt. Geology 24:703–706

Kirschvink J (1980) The least-squares line and plane and the analysis of palaeomagnetic data. Geophys J Int 62(3):699–718. https://doi.org/10.1111/j.1365-246X.1980.tb02601.x

Kitahara Y, Yamamoto Y, Ohno M, Kuwahara Y, Kameda S, Hatakeyama T (2018) Archeointensity estimates of a tenth-century kiln: first application of the Tsunakawa-Shaw paleointensity method to archeological relics. Earth Planets Space 70:79. https://doi.org/10.1186/s40623-018-0841-5

Kitahara Y, Nishiyama D, Ohno M, Yamamoto Y, Kuwahara Y, Hatakeyama T (2021) Construction of new archaeointensity reference curve for East Asia from 200 CE to 1100 CE. Phys Earth Planet Inter 310:106596. https://doi.org/10.1016/j.pepi.2020.106596

Korte M, Constable C (2011) Improving geomagnetic field reconstructions for 0–3 ka. Phys Earth Planet Inter 188:247–259. https://doi.org/10.1016/j.pepi.2011.06.017

Mochizuki N, Tsunakawa H, Oishi Y, Wakai S, Wakabayashi KI, Yamamoto Y (2004) Palaeointensity study of the Oshima 1986 lava in Japan: implications for the reliability of the Thellier and LTD-DHT Shaw methods. Phys Earth Planet Inter 146(3–4):395–416. https://doi.org/10.1016/j.pepi.2004.02.007

Nakamura K (1964) Volcano-stratigraphic study of Oshima Volcano Izu. Bull Earthq Res Inst 42:649–728

Nitta H, Saito T, Shitaoka Y (2020) Recent eruption history inferred from eruption ages of the two latest lava flows using multi-dating at Yokodake Volcano, Japan. Earth Planets Space 72(1):1–15. https://doi.org/10.1186/s40623-020-01220-3

Ohno Y, Iguchi A, Ijima M, Yasumoto K, Suzuki A (2022) Coastal ecological impacts from pumice rafts. Sci Rep 12:11187. https://doi.org/10.1038/s41598-022-14614-y

Okamura Y, Yuasa M, Kuramoto S, Ishihara T, Joshima M, Komazawa M (1999) Geological map Suruga Wan, GSJ Marine Geology Map Series, 52. Geol Surv Japan 132(5):439

Pavón-Carrasco FJ, Osete ML, Torta JM, De Santis A (2014) A geomagnetic field model for the Holocene based on archaeomagnetic and lava flow data. Earth Planet Sci Lett 388:98–109. https://doi.org/10.1016/j.epsl.2013.11.046

Prévot M, Mankinen EA, Gromme S, Lecaille A (1983) High paleointensities of the geomagnetic field from thermomagnetic studies on rift valley pillow basalts from the mid-Atlantic Ridge. J Geophys Res Solid Earth 88(B3):2316–2326. https://doi.org/10.1029/JB088iB03p02316

Riisager P, Riisager J, Zhao X, Coe RS (2003) Cretaceous geomagnetic paleointensities: Thellier experiments on Pillow lavas and Submarine basaltic

glass from the Ontong Java Plateau. Geochem Geophys Geosyst 4:8803. https://doi.org/10.1029/2003GC000611
Rolph TC, Shaw J (1985) A new method of palaeofield magnitude correction for thermally altered samples and its application to lower carboniferous lavas. Geophys J Int 80(3):773–781. https://doi.org/10.1111/j.1365-246X.1985.tb05124.x
Santos E, Trindade Y, Hartmann R, Hatakeyama GA, Terra-Nova T, Matsumoto F, Mitsumoto N, Gulmini J (2023) Archaeointensity record of weak field recurrence in Japan: new data from Late Yayoi and Kofun ceramic artefacts. Geophys J Int 233(2):950–963. https://doi.org/10.1093/gji/ggac498
Shaw J (1974) A new method of determining the magnitude of the palaeomagnetic field: application to five historic lavas and five archaeological samples. Geophys J Int 39(1):133–141. https://doi.org/10.1111/j.1365-246X.1974.tb05443.x
Tanaka H (1982) Geomagnetic paleointensities for the period 6000 to 3000 years bp determined from lavas and pyroclastic Flows in Japan. J Geomagnet Geoelectr 34(11–12):601–617. https://doi.org/10.5636/jgg.34.601.Tema
Tsunakawa H, Shaw J (1994) The Shaw method of palaeointensity determinations and its application to recent volcanic rocks. Geophys J Int 118(3):781–787. https://doi.org/10.1111/j.1365-246X.1994.tb03999.x
Yamamoto Y, Hoshi H (2008) Paleomagnetic and rock magnetic studies of the Sakurajima 1914 and 1946 andesitic lavas from Japan: a comparison of the LTD-DHT Shaw and Thellier paleointensity methods. Phys Earth Planet Inter 167(1–2):118–143. https://doi.org/10.1016/j.pepi.2008.03.006
Yamamoto Y, Tsunakawa H, Shibuya H (2003) Palaeointensity study of the Hawaiian 1960 lava: implications for possible causes of erroneously high intensities. Geophys J Int 153(1):263–276. https://doi.org/10.1046/j.1365-246X.2003.01909.x
Yoshihara A, Kondo A, Ohno M, Hamano Y (2003) Secular variation of the geomagnetic field intensity during the past 2000 years in Japan. Earth Planet Sci Lett 210:219–231. https://doi.org/10.1016/S0012-821X(03)00123-7
Yu Y (2012) High-fidelity paleointensity determination from historic volcanoes in Japan. J Geophys Res 117:B08101. https://doi.org/10.1029/2012JB009368
Yu Y, Tauxe L, Genevey A (2004) Toward an optimal geomagnetic field intensity determination technique. Geochem Geophys Geosyst 5:0207. https://doi.org/10.1029/2003GC000630

Publisher's Note